Document Version
Final published version

Licence
CC BY-NC-ND

Citation (APA)
Choi, Y. B., Park, J., Jung, W., Park, S., Ali, M. N., & Lee, G. H. (2026). Signatures of fractional Josephson effect in Josephson junctions based on the higher-order topological insulator WTe_2. *Current Applied Physics*, *86*, 141-147.
https://doi.org/10.1016/j.cap.2026.03.005

Current Applied Physics 86 (2026) 141–147

Contents lists available at ScienceDirect

Current Applied Physics

journal homepage: www.elsevier.com/locate/cap

Signatures of fractional Josephson effect in Josephson junctions based on the higher-order topological insulator WTe_2

Yong-Bin Choi [a,1], Jinho Park [a,b,1], Woochan Jung [a], Sein Park [a], Mazhar N. Ali [c,d], Gil-Ho Lee [a,e,*]

[a] Department of Physics, POSTECH, Pohang, Republic of Korea
[b] Department of Mechanical Engineering, Columbia University, New York, NY, 10027, USA
[c] Kavli Institute of Nanoscience, Delft University of Technology, Delft, Netherlands
[d] Department of Quantum Nanoscience, Delft University of Technology, Delft, Netherlands
[e] Asia Pacific Center for Theoretical Physics, Pohang, Republic of Korea

ARTICLE INFO

Keywords:
Josephson junction
Higher-order topological insulator
Shapiro step
Current-phase relationship

ABSTRACT

Higher-order topological insulators (HOTIs) represent a novel class of topological materials, characterised by the emergence of topological boundary modes at dimensions two or more lower than those of bulk materials. Recent experimental studies [1–4] have identified conducting channels at the hinges of HOTIs, although their topological nature remains unexplored. In this study, we investigated Shapiro steps in Al–WTe_2–Al proximity Josephson junctions (JJs) under microwave irradiation and examined the topological properties of the hinge states in WTe_2. Specifically, we analysed the microwave frequency dependence of the absence of the first Shapiro step in hinge-dominated JJs, which is consistent with a contribution from a 4π-periodic current–phase relationship characteristic of topological JJs. These findings encourage further research into topological superconductivity in superconducting hybrid devices based on HOTIs.

Three-dimensional (3D) higher-order topological insulators (HOTIs) represent a novel class of topological materials [1–22], characterised by topologically protected 1D conducting hinge states and topologically trivial and gapped 2D surface and 3D bulk states. Among the distinctive topological features of HOTIs, spin–momentum locking has garnered considerable attention across diverse fields, including condensed matter physics [1–24], photonics [25–29], and electrical circuit design [30]. Specifically, in condensed matter physics, the hinge states of HOTIs are under investigation for potential applications in spintronic devices [3,12,21] and superconducting Josephson diodes [22]. More recently, theoretical studies have extended higher-order topology to 2D platforms, including magnetic systems and Floquet-driven settings, where tunable topological phase transitions provide routes to quantum anomalous Hall phases and motivate orbitronic and spintronic device concepts [31–34]. Topological superconductivity is theorised to originate from interactions between hinge states and *s*-wave superconductors, as proposed in the context of topological materials [35–37], quantum spin Hall systems [38], and semiconductors [39,40]. However, experimental observations of HOTIs are complicated by the effects of topologically trivial surface and bulk states [1–4,7,8,12–16], which hinder interpretation and limit direct evidence. Nevertheless, numerous investigations into HOTIs and their properties, including studies on pre-patterned Josephson junctions (JJs) with tungsten ditelluride (WTe_2) [7–10], switching current distributions in bismuth [4] and WTe_2 [8], and spin transport in Cd_3As_2 [12], are underway.

Recent theoretical studies report that WTe_2, initially identified as a type-II Weyl semimetal [41], may also exhibit features characteristic of a HOTI [6]. Specifically, a higher-order topological phase can emerge when two adjacent Weyl points merge in momentum space, opening a surface state gap within a crystal structure that preserves mirror symmetry [6]. In the monolayer limit of WTe_2, 1D topological edge states, characteristic of a quantum spin Hall insulator, have been observed in transport measurements [42–44]. Similarly, in the multilayer limit of WTe_2, previous studies have demonstrated the presence of conducting states at the hinges of WTe_2 crystals by analysing the magnetic field interference pattern of the Josephson critical current in WTe_2-based JJs and providing a spatial distribution of the Josephson current density [2,7–9]. This technique has proven to be a powerful tool for investigating

---

* Corresponding author. Department of Physics, POSTECH, Pohang, Republic of Korea.
E-mail address: lghman@postech.ac.kr (G.-H. Lee).

[1] These authors contributed equally.

https://doi.org/10.1016/j.cap.2026.03.005
Received 11 December 2025; Received in revised form 5 March 2026; Accepted 8 March 2026

surface or hinge states, even in the presence of dominant bulk conduction. Furthermore, scanning tunnelling microscopy-based studies have provided evidence of hinge states at the step edges of WTe_2 crystals [45], as well as bismuth crystals and their alloys [1,14–16,19,20]. However, the topological nature of such hinge states is yet to be conclusively verified.

JJs offer a valuable platform for investigating the topological properties of hinge states. Specifically, when two *s*-wave superconducting leads are coupled by topologically protected conduction channels, the Andreev bound state (ABS) and the corresponding current phase relationship (CPR), $I_s = (2e/\hbar)\, dE_{ABS}/d\varphi$, exhibit 4π periodicity, unlike the 2π periodicity observed in topologically trivial JJs [35–40,46–49]. In the above equation, $\hbar = h/2\pi$ represents the reduced Planck constant, e denotes the electron charge, φ represents the macroscopic quantum phase difference between two superconductors, and E_{ABS} denotes the energy of the ABS. The 4π-periodic ABS, linked to the fractional Josephson effect, results from the parity conservation of Majorana zero modes [35–40,46–56] (Fig. 1a). This phenomenon is experimentally observed through Shapiro step measurements under microwave irradiation. For non-topological JJs with a 2π-periodic ABS, Shapiro steps appear at bias voltages equivalent to integer multiples of $V_0 = hf/2e$, where f denotes the microwave frequency. Conversely, for topological JJs with a 4π-periodic ABS, Shapiro steps occur at bias voltages equivalent to even multiples of V_0, resulting in the absence of all odd-order Shapiro steps in the case of purely 4π-periodic CPR (Fig. 1b). Experimentally, the disappearance of the first Shapiro step has been observed in JJs fabricated from various topological materials, including strong spin–orbit-coupled semiconducting nanowires [50], 2D HgTe quantum wells [51], 3D topological insulators [52–55], and Dirac semimetals [56]. Possible non-topological mechanisms [57–62] that may also lead to missing Shapiro steps will be discussed later in the manuscript.

In this study, we explored the topological nature of hinge states in multilayer WTe_2 by analysing Shapiro steps in WTe_2-based JJs. Aluminium superconducting leads were coupled to multilayer WTe_2 flakes in two electrode configurations: a bJJ and an hJJ, as depicted in Fig. 1c–e. To specifically investigate the topological hinge state, we fabricated JJs aligned along the a-axis of the crystals, where hinge states are theoretically and experimentally known to remain spatially well-localized at the crystal hinges [2]. These configurations allow a comparative investigation of Shapiro steps, highlighting variations in the hinge-to-bulk contribution ratio. The first Shapiro step is missing in the hJJ but not in the bJJ, suggesting a possible topological contribution of the hinge states in multilayer WTe_2. The dependence of this first Shapiro step missing in the hJJ on microwave power and frequency is consistent with the predictions of the resistively and capacitively shunted junction (RCSJ) model including a 4π-periodic contribution. Furthermore, the magnitude of the 4π-periodic Josephson current, estimated from Shapiro step measurements, is comparable to the Josephson current flowing through the hinge states. This current is derived from the edge-enhancement of the Josephson current density, as determined from magnetic interference patterns [2]. These observations are consistent with a scenario in which hinge states host a significant topological contribution, and they motivate further exploration of Majorana physics in layered topological materials.

The JJs were fabricated using a 13-nm-thick multilayer WTe_2 crystal, with the Josephson current flowing along the *a*-axis of the crystal. The

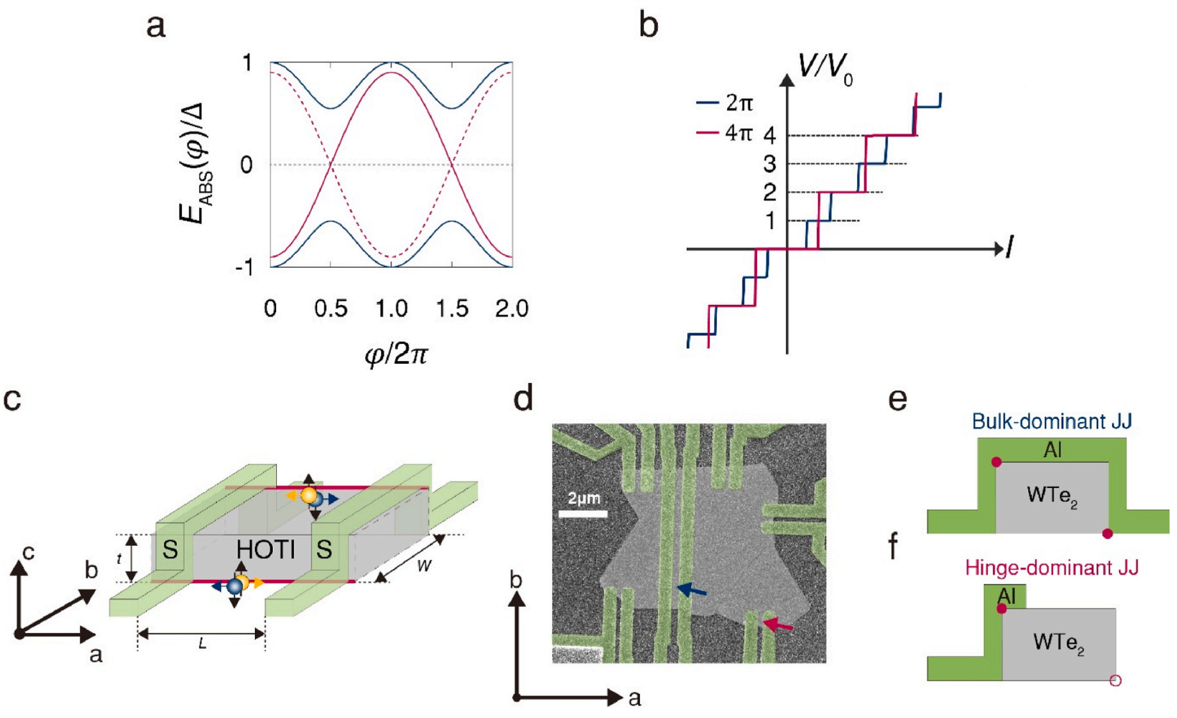

Fig. 1. Schematic and experimental representations of HOTIs and JJs. a, Energy spectra of the ABSs, E_{ABS}, as a function of the macroscopic quantum phase difference, φ, between two superconductors. Here, Δ represents the superconducting gap. Gapless 4π-periodic ABSs (red solid and dashed lines) and gapped 2π-periodic ABSs (blue solid lines) are illustrated. **b,** Numerically derived current–voltage characteristics depicting Shapiro steps under microwave irradiation for purely 2π- and purely 4π-periodic ABSs. The voltage is normalised by $V_0 = hf/2e$, where h denotes Planck constant, f represents the microwave frequency, and e denotes the electron charge. **c,** Schematic of a JJ based on a HOTI. Spin-up (yellow) and spin-down (blue) electrons travel in opposite directions along the topological hinge state (red lines), which is in contact with superconducting (S) electrodes (green). W, L, and t denote the junction width, junction length, and thickness of the JJ, respectively. **d,** False-colour scanning electron micrograph of the device. Bulk-dominant JJs (bJJ) and hinge-dominant JJs (hJJ) are indicated by blue and red arrows, respectively. **e, f,** Schematic side views of bJJ and hJJ, respectively. Grey regions represent WTe_2 flakes, while red regions indicate hinge states. Filled (solid) and empty (void) red circles depict hinge states coupled and decoupled with aluminium superconducting electrodes, respectively. (For interpretation of the references to colour in this figure legend, the reader is referred to the Web version of this article.)

junction widths of the bJJ and hJJ were 5.8 μm and 0.65 μm, respectively (Fig. 2a and d). Both these JJs had the same channel length of $L = 0.2$ μm. The critical current (I_c) and normal-state resistance (R_N) were 2.73 μA and 4.40 Ω for the bJJ and 0.53 μA and 25.7 Ω for the hJJ, respectively. Despite the differences in junction geometry between the bJJ and hJJ, the Josephson coupling strengths, represented by I_cR_N products, were similar for both: 12.0 μV for the bJJ and 13.6 μV for the hJJ, as summarised in Table S1 in Supplementary Section S2. The aluminium (Al) superconducting gap was estimated as $\Delta_{Al} = 0.12$ meV, based on the relation $\Delta_{Al} = 1.763 \cdot k_B T_{c,Al}$ and a critical temperature of $T_{c,Al} = 0.75$ K. To confirm the presence of hinge states in the WTe$_2$ crystal, we analysed the magnetic field interference behaviour of I_c, as reported in our previous study [2] (see Fig. S1). Next, we performed Shapiro step measurements by recording the I–V characteristics at 20 mK while irradiating the JJ devices with microwaves. The JJs exhibited small hysteresis in their I–V characteristics: $I_c/I_r \sim 1.03$ for the bJJ and 1.14 for the hJJ. This indicates that the junctions are marginally underdamped, with an estimated McCumber parameter $\beta = 2eI_cR_N^2C/\hbar$ from the RCSJ model of 1.1 for the bJJ and 1.6 for the hJJ (see Fig. S2). Here, R_N and C denote normal-state resistance and capacitance, respectively.

The measured Shapiro steps in the bJJ, which has a significant bulk contribution (Fig. 2a), resemble the ordinary Shapiro steps observed in conventional 2π-periodic JJs. Fig. 2b illustrates the I–V characteristics of the bJJ under microwave irradiation at different nominal values of I_{ac}. The value of I_{ac} was estimated from the microwave power (P) at the microwave source output using the relation $I_{ac} \equiv 10^{[P/(20\ \mathrm{dBm})]}$. As depicted in the figure, Shapiro steps gradually appear in the I–V characteristics with increasing I_{ac}. In the upper panel of Fig. 2c, colours represent the step width (I_s), normalised by I_c. All integer multiples of V_0 (*i.e.*, voltage steps $V_n = nV_0$ for integer n) are highlighted in yellow. Notably, the first step ($V_{n=1}$), indicated by the red arrow, remains prominent across all frequencies (see Fig. S3), resembling the behaviour of ordinary Shapiro steps. The lower panel of Fig. 2c presents horizontal line cuts from the upper panel at $n = 0, 1$, and 2, marked by dashed lines. These cuts illustrate the evolution of the step width with I_{ac}. The amplitudes of the first and second steps evolve continuously, following Bessel function behaviour. Furthermore, the first lobe of the $n = 1$ step peaks at a lower I_{ac} than that of the $n = 2$ step. Moreover, the ratio of w_1 to w_2 ($Q_{12} = w_1/w_2$) is 1.04, which is greater than one. Here, w_1 and w_2 denote the amplitude maxima of the first lobes of the voltage steps $n = 1$ and $n = 2$, respectively. Overall, the bJJ exhibits ordinary Shapiro steps consistent with bulk-dominant transport; this does not exclude possible hinge contributions, which may be effectively masked by the bulk/surface supercurrent.

In the hJJ (Fig. 2d), which has a larger hinge-to-bulk contribution ratio than the bJJ, the first Shapiro step is entirely absent as shown in Fig. 2e. Similar results were observed from two additional devices (see Fig. S4). For comparison, representative Shapiro step measurements from b-axis junctions and related discussion are provided in Supplementary Section S6 (Figs. S5–S9). In the upper panel of Fig. 2f, the region near $V/V_0 = 1$, marked by the red arrow, appears dark blue, suggesting that I_s is close to zero. The lower panel of Fig. 2f illustrates that the I_s of the first step remains nearly zero until I_{ac} approaches 0.43, where the second lobe of the $n = 1$ step begins to emerge. Conversely, the I_s of the second step evolves continuously from a lower I_{ac}. Quantitative analysis reveals that $w_1 \sim 0.004$ and $w_2 \sim 0.07$, yielding $Q_{12} = 0.057$, a value considerably smaller than one. In this measurement, $w_1 \times I_c \sim 2$ nA is comparable to the minimum current step (2 nA). Additional frequency dependencies of the Shapiro steps from other hJJs are provided in Supplementary Section S7 (Figs. S10–S15).

We investigated the dependence of Shapiro steps on microwave frequency in the hJJ and compared the results with the outcomes of numerical calculations. Fig. 3 presents experimentally measured Shapiro steps alongside those derived from numerical calculations based on the RCSJ model, using the CPR of $I_J(\phi) = I_{4\pi}\sin(\phi/2) + I_{2\pi}\sin(\phi)$. Here, I_J represents the Josephson current, and $I_{2\pi}$ and $I_{4\pi}$ denote the 2π- and 4π-periodic Josephson currents, respectively. The numerical calculations were performed using $\beta = 1.6$, estimated from the I–V characteristics of the hJJ, and $\alpha = 0.20$, which best matches the experimental data (see Fig. S16 for numerical results at different α). Here, $\alpha = I_{4\pi}/I_{2\pi}$ represents the ratio of the 4π-periodic Josephson current to the 2π-periodic one. In Fig. 3a, the first lobe of the $n = 1$ step is entirely absent. As f increases, the first Shapiro step becomes faintly visible. At $f = 1.2$ GHz (Fig. 3b), the first Shapiro step, indicated by the white arrow, faintly appears near the $n = 0$ step. As f increases further, the Shapiro steps evolve into a standard form, displaying all integer steps. This behaviour is consistent with theoretical predictions [46–48] (Fig. 3e–h) and

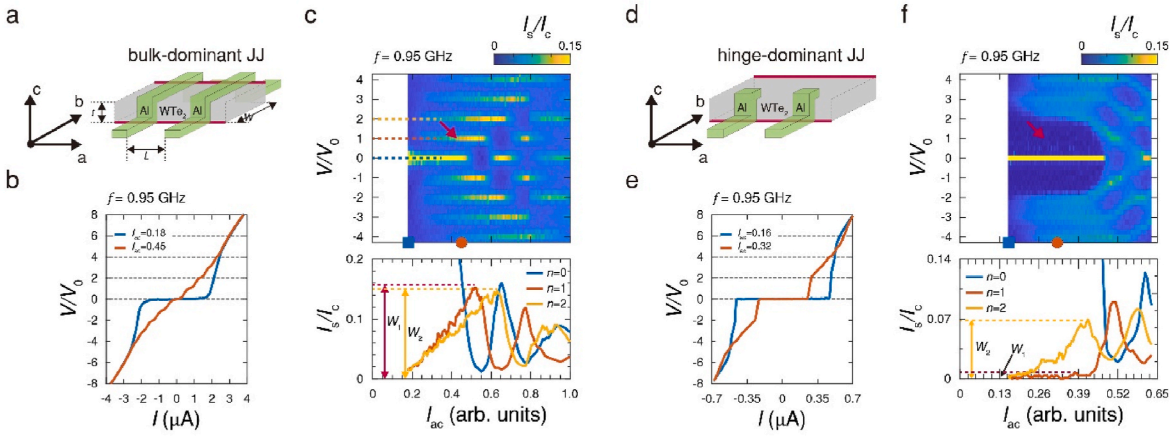

Fig. 2. Shapiro steps in bJJ and hJJ. a, d, Schematic representations of (**a**) a bJJ and (**d**) an hJJ. Topological hinge states (red solid lines) are connected to aluminium superconducting electrodes (green). W, L, and t represent the junction width, junction length, and thickness of the JJ, respectively. **b, e,** Current (I)–voltage (V) characteristics of (**b**) the bJJ with a microwave frequency $f \simeq 0.95$ GHz and (**e**) the hJJ with $f \simeq 0.95$ GHz at different nominal microwave alternating current (ac) amplitudes (I_{ac}). I–V measurements were performed by sweeping the bias current from negative to positive with constant current steps. The I_{ac} values correspond to symbols in (**c**) and (**f**): square (blue) and circle (red). **c, f,** (Upper panels) Shapiro steps as a function of I_{ac} and normalised voltage (V/V_0) for the bJJ (**c**) and hJJ (**f**). Here, $V_0 = hf/2e$, where h denotes Planck's constant, and e is the electron charge. The colour map represents the width of the current step (I_s) at a given normalised voltage step ($\Delta V/V_0 = 0.25$), normalised by the critical current (I_c). The normalised voltage $V/V_0 = 1$ is indicated by a red arrow. (Lower panels) Horizontal line cuts of (**c**) and (**f**) at $V/V_0 = 0$ (blue), $V/V_0 = 1$ (red), and $V/V_0 = 2$ (orange). w_1 and w_2 represent the maximum I_s/I_c values for the first lobes of $V/V_0 = 1$ and $V/V_0 = 2$ steps, respectively. (For interpretation of the references to colour in this figure legend, the reader is referred to the Web version of this article.)

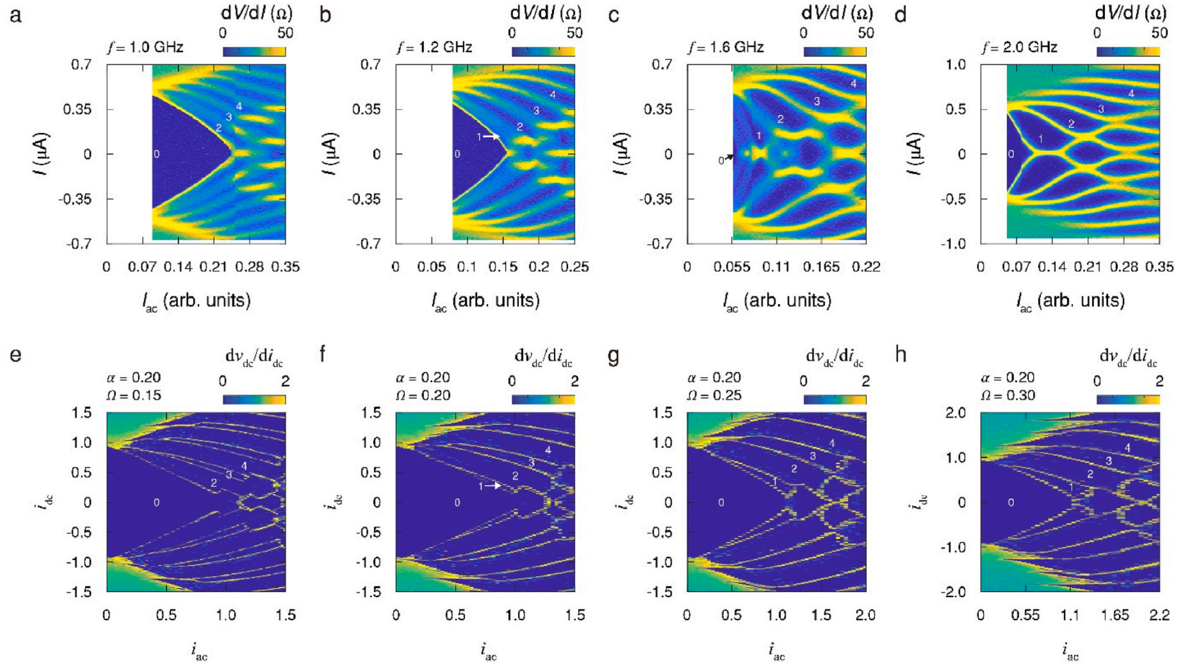

Fig. 3. Frequency dependence of Shapiro steps in the hJJ. **a–d,** Shapiro steps measured in the hJJ as a function of I_{ac} and bias current I at different microwave frequencies : (**a**) $f = 1.0$ GHz, (**b**) $f = 1.2$ GHz, (**c**) $f = 1.6$ GHz, and (**d**) $f = 2.0$ GHz. Colours indicate the differential resistance. **e–h,** Numerically calculated Shapiro steps for $\beta = 1.6$ and $\alpha = 0.20$ as functions of i_{ac} and bias current (i_{dc}) at different dimensionless frequencies ($\Omega = hf/2eI_cR_N$): (**e**) $\Omega = 0.15$, (**f**) $\Omega = 0.20$, (**g**) $\Omega = 0.25$, and (**h**) $\Omega = 0.30$. Here, α denotes the ratio of the 4π-periodic Josephson current to the 2π-periodic Josephson current, and $\beta = 2eI_cR_N^2C/\hbar$ represents the McCumber parameter . v_{dc} denotes the dc voltage applied across the junction normalised by I_cR, and i_{ac} and i_{dc} represent the normalised ac and dc current, respectively. (For interpretation of the references to colour in this figure legend, the reader is referred to the Web version of this article.)

experimental findings from previous studies [50–56] (see Fig. S17 for Shapiro steps as a function of I_{ac} and V/V_0).

The experimental results show broader boundaries between adjacent steps compared to the numerical calculations. This discrepancy is likely attributed to Joule heating, arising from both the dc and microwave radiation introduced through the antenna. The resulting increase in electron temperature alters the phase dynamics of particles in the JJs. Consequently, the slopes of the plateaux where Shapiro steps occur become less distinct, and the sharp voltage transitions between steps appear smoother. To mitigate the effects of Joule heating, we focus on the ratio between the first lobes of the $n = 1$ and $n = 2$ steps, represented by Q_{12}, which is evaluated under conditions of low dc and ac values. Notably, this low-current regime underscores the significant influence of the 4π-periodic CPR on Shapiro steps, as supported by previous studies [49]. The missing of higher-order odd Shapiro steps (e.g., $n \geq 3$) becomes increasingly difficult to observe due to finite 2π-periodic component in CPR (see Supplementary Section S10).

Fig. 4a and b display the experimentally measured Q_{12} values as functions of Ω for the bJJ and hJJ, respectively, alongside the numerically calculated values at various α. Both experimental and numerical results extend down to $\Omega \sim 0.05$ (corresponding to $f \sim 0.3$ GHz), below which the Shapiro step voltage $V_0 < 0.6$ μV becomes too small to be measured experimentally. As Ω decreases, Q_{12} approaches zero for $\alpha \neq 0$ or approaches a non-zero value of approximately 0.7 for $\beta = 1.1$ and 0.5 for $\beta = 1.6$ when $\alpha = 0$. Moreover, Q_{12} tends to decrease as α or β increases for a given Ω (see Fig. S18). At higher frequencies ($\Omega > 0.3$), the experimentally measured Q_{12} is consistently larger than the numerical values in both the bJJ and hJJ, indicating additional effects beyond the

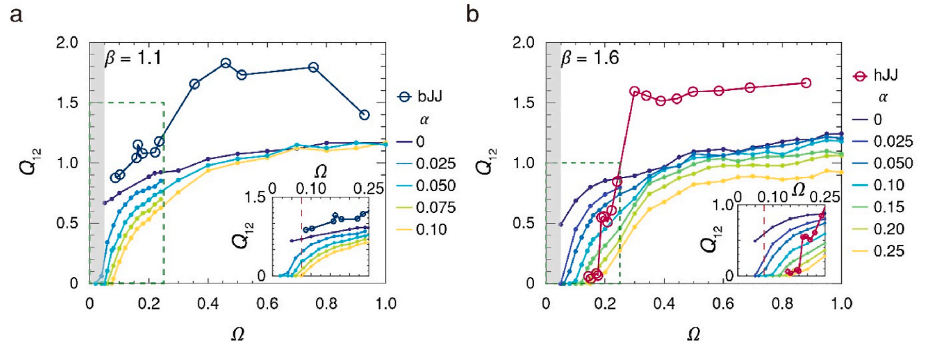

Fig. 4. Microwave frequency dependence of Q_{12}. Microwave frequency dependence of Q_{12} as a function of the dimensionless frequency for (**a**) $\beta = 1.1$ and (**b**) $\beta = 1.6$. Here, α denotes the ratio of the 4π-periodic Josephson current to the 2π-periodic current, $\beta = 2eI_cR_N^2C/\hbar$ represents the McCumber parameter, $Q_{12} = w_1/w_2$, and $\Omega = hf/2eI_cR_N$ represents the dimensionless frequency. The solid lines represent the numerically calculated Q_{12}, while the solid lines with circles indicate experimental results. The grey area marks the frequency range that cannot be measured experimentally. The green dashed box highlights the zoomed-in region shown in the inset. Inset: Enlarged view of the region from $\Omega = 0$ to $\Omega = 0.25$. The red dashed line in the inset corresponds to $\Omega = 0.075$. (For interpretation of the references to colour in this figure legend, the reader is referred to the Web version of this article.)

minimal RCSJ model, such as electron heating and high-frequency circuit dynamics. The Joule heating power (P) is proportional to n^2 ($P\propto V_n{}^2\propto n^2f^2$) at the n-th Shapiro step; hence, w_2, measured at the $n = 2$ step, is more affected by elevated electron temperature than w_1, measured at $n = 1$. This results in an overestimation of Q_{12}, which would otherwise diminish at lower f. The value of Ω below which Q_{12} vanishes is used as a proxy for estimating α, following the approach of previous studies [49,52]. For the hJJ, this yields $\alpha_{\mathrm{hJJ}} \cong 0.2$, which corresponds to $I_{4\pi} \cong 93$ nA. Similar $\alpha = 0.10 - 0.25$ values are obtained for other hJJs (see Fig. S19). This $I_{4\pi}$ magnitude is consistent with, and does not exceed, the edge-enhanced Josephson supercurrent inferred from magnetic interference patterns extracted from the bJJ on the same $\mathrm{WTe_2}$ device (see Supplementary Section S1), supporting the internal consistency of our interpretation. Since the inversion has limited spatial resolution and may mix several edge or terrace channels, this comparison should be regarded as an order-of-magnitude consistency check rather than an independent determination of hinge supercurrent. The Josephson current mediated by a single hinge state is estimated as $I_{\mathrm{J,h}} = 15$ nA, considering the short ballistic junction limit $I_{\mathrm{J,h}}R_{\mathrm{N,h}} = \pi\Delta_{\mathrm{Al}}/e$, where $R_{\mathrm{N,h}} = h/e^2$ denotes the normal-state resistance for a single hinge state. The $I_{4\pi}$ value derived from the Shapiro step analysis likely originates from multiple hinge states located at the terraces of the $\mathrm{WTe_2}$ crystal, which may have formed during mechanical exfoliation. Assuming that each of the two crystal edges (upper and lower) of the bJJ has an $I_{4\pi}$ comparable to that of the hJJ, $\alpha_{\mathrm{bJJ}} = 0.07$ can be estimated for the bJJ. This indicates that the complete missing of the first Shapiro step ($Q_{12} = 0$) may also occur in the bJJ at $f < 0.4$ GHz. However, at such low microwave frequencies, V_0 becomes as small as 0.8 μV, making experimental measurement extremely challenging due to thermal fluctuations caused by Joule heating and/or external electrical noise. In addition, Joule heating near the steps may further broaden the response and artificially increase Q_{12}. Consequently, potential topological hinge states in the bJJ are obscured by dominant contributions from trivial conduction states.

Our next analysis focused on determining whether the complete missing of the first Shapiro step in the hJJ originates from topologically trivial mechanisms. The missing of the first Shapiro step can result from topologically trivial factors [57–59,61,62] such as Landau−Zener transitions (LZT) or the underdamped nature of JJs. First, the LZT is a non-adiabatic transition triggered by microwaves, which can create an ABS bandgap near $\phi \sim \pi$. The probability of the LZT [59,63] is defined as $P_{\mathrm{LZT}} = \exp\left(-\pi\frac{(1-D)\Delta}{eV_{\mathrm{LZT}}}\right)$, where D denotes the junction transparency, and V_{LZT} represents the junction voltage at $\phi = \pi$. Given the similar Josephson coupling strengths of the bJJ and hJJ, D is also likely comparable [64]. Moreover, Shapiro steps for both junctions were measured within a similar microwave frequency range. Therefore, it is unlikely that LZT alone is responsible for the missing first step only in the hJJ, although a contribution from highly transmitting modes cannot be completely ruled out. Second, a recent study [62] suggested that spurious inductance can induce phase dynamics leading to period doubling and missing odd Shapiro steps. However, our experimental configuration is fundamentally different, as our devices do not have an external shunt resistor and inductor as depicted in Fig. S20. Therefore, the specific inductive mechanism discussed in Ref. [62] is less directly relevant in our case. A quantitative assessment would require a full ac circuit characterisation and numerical simulations in a realistic equivalent circuit, which are beyond the scope of this work (see Supplementary Section S12). Finally, we evaluated the underdamped nature of the JJs using our previous RCSJ model calculations [49]. At sufficiently low Ω, Q_{12} decreases with increasing β, even when $\alpha = 0$. However, in the absence of a 4π-periodic Josephson current, the complete missing of the first Shapiro step ($Q_{12} = 0$) does not occur for $\beta \leq 3$. Given that $\beta = 1.6$ for the hJJ is considerably smaller than three, the first Shapiro step missing observed in the hJJ is unlikely to be explained solely by the underdamped nature of the junction within our modelling. Taken together, these considerations show that none of the known non-topological mechanisms can be strictly ruled out by our present data, but they face significant difficulties in reproducing the robust and frequency-selective suppression of the first step only in the hinge-dominated junctions. In contrast, a finite 4π-periodic contribution within an extended RCSJ model captures these key features in a simple and self-consistent way. We therefore regard the scenario with a 4π-periodic contribution as the most natural interpretation of our data, while keeping in mind that non-topological origins cannot yet be completely excluded.

In this study, we fabricated two types of $\mathrm{WTe_2}$ JJs: a bJJ and an hJJ, with current flowing along the a-axis of the crystal. To investigate the topological nature of the hinge states, we analysed the Shapiro step behaviour of these junctions. Under microwave irradiation, the hJJ, with reduced conduction contributions from topologically trivial surface and bulk states, exhibits a missing first Shapiro step, which may be associated with a fractional Josephson effect. In contrast, the bJJ exhibits the first Shapiro step, which is attributed to the significant conduction contributions from topologically trivial states. We further examined the microwave frequency and power dependencies of the Shapiro steps and provided quantitative explanations using numerical calculations based on the RCSJ model. Notably, the estimated value of the 4π-periodic Josephson current in the hJJ is comparable in magnitude to the edge-enhanced Josephson supercurrent attributed to hinge-like channels, as inferred from magnetic field interference patterns. This result is consistent with a topological contribution from the hinge states in $\mathrm{WTe_2}$. Our findings suggest the topological nature of the hinge states; however, non-topological mechanisms such as Landau-Zener transitions, bias-dependent dissipation, or inductive phase dynamics cannot yet be completely excluded. Further experiments, including Josephson radiation [65–67] or bimodal switching current distribution [68], will be essential to clarify the microscopic origin unambiguously.

1. Methods

Device fabrication. A multilayer $\mathrm{WTe_2}$ crystal was mechanically exfoliated onto a silicon substrate with a 280-nm-thick insulating layer of $\mathrm{SiO_2}$. The crystal thickness was confirmed to be 13 nm using atomic force microscopy (using an XE-7 from Park Systems). To remove any contamination from the topmost layers of $\mathrm{WTe_2}$ flakes, *in situ* argon ion etching was conducted before metal deposition to eliminate $\mathrm{WTe_2}$ surface layers potentially oxidised in ambient air. Ti/Al/Au (5 nm/60 nm/5 nm) electrodes were deposited through evaporation to facilitate the study of superconducting transport. The Ti layer improved the adhesion of the electrodes to $\mathrm{WTe_2}$, while the Au layer protected the aluminium superconducting electrodes from oxidation. During evaporation, the chamber pressure was maintained below 2×10^{-7} Torr. To minimise degradation, the multilayer $\mathrm{WTe_2}$ crystal was exposed to poly(methyl methacrylate) polymer only once during the fabrication process.

Measurement and analysis. All electrical measurements were performed in a dilution refrigerator at base temperatures of approximately 20 mK. A dc current bias was applied to the device, and the resulting dc voltage was measured using a low-noise preamplifier (ITHACO 1201) and recorded with a digital multimeter (Keithley 2000). Each I–V measurement was repeated three times and ensemble-averaged to reduce noise and enhance reliability. To analyse the Shapiro steps, the measured voltage was converted into normalised step indices $n = V/V_0$, where $V_0 = hf/2e$. Due to thermal broadening and measurement noise, a finite window of width 0.25 in n was defined around each integer step. Within each such window (i.e., $n \pm 0.125$), the number of I–V data points was counted and multiplied by the current resolution dI to estimate the total current contribution I_{s} associated with the step. The resulting value was then normalised by the junction's critical current I_{c} to yield the dimensionless step width $I_{\mathrm{s}}/I_{\mathrm{c}}$.

Declaration of competing interest

The authors declare that they have no known competing financial interests or personal relationships that could have appeared to influence the work reported in this paper.

Acknowledgement

Half of this research was supported by the Nano and Material Technology Development Program through the National Research Foundation of Korea (NRF), funded by the Ministry of Science and ICT (No. RS-2024-00444725). Additional support was provided by other NRF grants (Nos. RS-2022-NR068223, RS-2024-00393599, RS-2024-00442710) and the ITRC program (IITP-2025-RS-2022-00164799), also funded by the Ministry of Science and ICT. Further support was received from Agency for Defense Development funded by Defense Acquisition Program Administration (DAPA) (UI257011TE), Samsung Science and Technology Foundation (SSTF-BA2101-06, SSTF-BA2401-03), and Samsung Electronics Co., Ltd. (IO201207-07801-01).

Appendix A. Supplementary data

Supplementary data to this article can be found online at https://doi.org/10.1016/j.cap.2026.03.005.

References

[1] F. Schindler, et al., Higher-order topology in bismuth, Nat. Phys. 14 (2018) 918–924.
[2] Y.-B. Choi, et al., Evidence of higher-order topology in multilayer WTe_2 from Josephson coupling through anisotropic Hinge states, Nat. Mater. 19 (2020) 974–979.
[3] J. Lee, et al., Spinful Hinge states in the higher-order topological insulators WTe_2, Nat. Commun. 14 (2023) 1801.
[4] A. Bernard, et al., Long-lived andreev states as evidence for protected Hinge modes in a bismuth nanoring josephson junction, Nat. Phys. 19 (2023) 358–364.
[5] F. Schindler, et al., Higher-order topological insulators, Sci. Adv. 4 (2018) eaat0346.
[6] Z. Wang, et al., Higher-order topology, monopole nodal lines, and the origin of large fermi arcs in transition metal dichalcogenides XTe_2 (X=Mo,W), Phys. Rev. Lett. 123 (2019) 186401.
[7] A. Kononov, et al., One-dimensional edge transport in few-layer WTe_2, Nano Lett. 20 (2020) 4228–4233.
[8] M. Endres, et al., Current-phase relation of a WTe_2 josephson junction, Nano Lett. 23 (2023) 4654–4659.
[9] A. Kononov, et al., Superconductivity in type-II Weyl-semimetal WTe_2 induced by a normal metal contact, J. Appl. Phys. 129 (2021) 113903.
[10] M. Endres, et al., Transparent josephson junctions in higher-order topological insulator WTe_2 via Pd diffusion, Phys. Rev. Mater. 6 (2022) L081201.
[11] B.J. Wieder, et al., Strong and fragile topological dirac semimetals with higher-order fermi arcs, Nat. Commun. 11 (2020) 627.
[12] A.Q. Wang, et al., Topological nature of higher-order Hinge states revealed by spin transport, Sci. Bull. 67 (2022) 788–793.
[13] T. Le, et al., Magnetic field filtering of the boundary supercurrent in unconventional metal $NiTe_2$-based josephson junctions, Nat. Commun. 15 (2024) 2785.
[14] B. Jack, et al., Observation of a majorana zero mode in a topologically protected edge channel, Science 364 (2019) 1255–1259.
[15] L. Aggarwal, et al., Evidence for higher order topology in Bi and $Bi_{0.92}Sb_{0.08}$, Nat. Commun. 12 (2021) 4420.
[16] T. Zhang, et al., Scanning tunneling microscopy observation of the Hinge states of bismuth nanocrystals, Phys. Rev. B 108 (2023) 085422.
[17] M.S. Hossain, et al., Quantum transport response of topological Hinge modes, Nat. Phys. 20 (2024) 776–782.
[18] R. Noguchi, et al., Evidence for a higher-order topological insulator in a three-dimensional material built from van der Waals stacking of bismuth-halide chains, Nat. Mater. 20 (2021) 473–479.
[19] N. Shumiya, et al., Evidence of a room-temperature quantum spin hall edge state in a higher-order topological insulator, Nat. Mater. 21 (2022) 1111–1115.
[20] J. Han, et al., Quasi-one-dimensional topological material Bi_4X_4(X=Br,I), Adv. Phys.:X 7 (2022) 2057234.
[21] W. Zhao, et al., Topological electronic structure and spin texture of quasi-one-dimensional higher-order topological insulator Bi_4Br_4, Nat. Commun. 14 (2023) 8089.
[22] Y. Li, et al., Interfering josephson diode effect in $Ta_2Pd_3Te_5$ asymmetric edge interferometer, Nat. Commun. 15 (2024) 9031.
[23] M.J. Park, et al., Higher-order topological insulator in twisted bilayer graphene, Phys. Rev. Lett. 123 (2019) 216803.
[24] E. Lee, et al., Two-dimensional higher-order topology in monolayer graphdiyne, npj Quantum Mater. 5 (2020) 1.
[25] J. Noh, et al., Topological protection of photonic mid-gap defect modes, Nat. Photonics 12 (2018) 408–415.
[26] C.W. Peterson, et al., A quantized microwave quadrupole insulator with topologically protected corner states, Nature 555 (2018) 346–350.
[27] M. Serra-Garcia, et al., Observation of a phononic quadrupole topological insulator, Nature 555 (2018) 342–345.
[28] M. Kim, et al., Recent advances in 2D, 3D and higher-order topological photonics, Light Sci. Appl. 9 (2020) 130.
[29] H. Gao, et al., Non-hermitian route to higher-order topology in an acoustic crystal, Nat. Commun. 12 (2021) 1888.
[30] S. Imhof, et al., Topolectrical-circuit realization of topological corner modes, Nat. Phys. 14 (2018) 925–929.
[31] R. Li, et al., Robust second-order topological insulators with giant Valley polarization in two-dimensional honeycomb ferromagnets, Nano Lett. 23 (2023) 91–97.
[32] Z. Chen, et al., Topology-engineered orbital hall effect in two-dimensional ferromagnets, Nano Lett. 24 (2024) 4826–4833.
[33] X. Zou, et al., Floquet quantum anomalous hall effect with In-Plane magnetization in two-dimensional altermagnets, ACS Nano 19 (2025) 35575–35580.
[34] X. Feng, et al., Engineering quantum anomalous hall effect with a high chern number in nonmagnetic second-order topological insulator, Adv. Funct. Mater. 35 (2025) 2501934.
[35] L. Fu, C.L. Kane, Superconducting proximity effect and Majorana fermions at the surface of a topological insulator, Phys. Rev. Lett. 100 (2008) 096407.
[36] J. Alicea, New directions in the pursuit of Majorana fermions in solid state systems, Rep. Prog. Phys. 75 (2012) 076501.
[37] A. Chen, et al., Josephson current signatures of Majorana flat bands on the surface of time-reversal-invariant Weyl and Dirac semimetals, Phys. Rev. B 95 (2017) 174505.
[38] L. Fu, C.L. Kane, Josephson current and noise at a superconductor/quantum-spin-hall-nsulator/superconductor junction, Phys. Rev. B 79 (2009) 161408.
[39] R.M. Lutchyn, et al., Majorana fermions and a topological phase transition in semiconductor-superconductor heterostructures, Phys. Rev. Lett. 105 (2010) 077001.
[40] B. van Heck, et al., Coulomb stability of the 4π-periodic Josephson effect of Majorana fermions, Phys. Rev. B 84 (2011) 180502(R).
[41] A.A. Soluyanov, et al., Type-II Weyl semimetals, Nature 527 (2015) 495–498.
[42] Z. Fei, et al., Edge conduction in monolayer WTe_2, Nat. Phys. 13 (2017) 677–682.
[43] S. Tang, et al., Quantum spin Hall state in monolayer 1T'-WTe_2, Nat. Phys. 13 (2017) 683–687.
[44] S. Wu, et al., Observation of the quantum spin Hall effect up to 100 kelvin in a monolayer crystal, Science 359 (2018) 76.
[45] L. Peng, et al., Observation of topological states residing at step edges of WTe_2, Nat. Commun. 8 (2017) 659.
[46] F. Domínguez, et al., Josephson junction dynamics in the presence of 2π- and 4π-periodic supercurrents, Phys. Rev. B 95 (2017) 195430.
[47] J. Picó-Cortés, et al., Signatures of a 4π-periodic supercurrent in the voltage response of capacitively shunted topological Josephson junctions, Phys. Rev. B 96 (2017) 125438.
[48] Y.-H. Li, et al., Doubled Shapiro steps in a topological Josephson junction, Phys. Rev. B 97 (2018) 045423.
[49] J. Park, et al., Characterization of Shapiro steps in the presence of a 4π-periodic Josephson current, Phys. Rev. B 103 (2021) 235428.
[50] L.P. Rokhinson, et al., The fractional a.c. Josephson effect in a semiconductor–superconductor nanowire as a signature of Majorana particles, Nat. Phys. 8 (2012) 795–799.
[51] E. Bocquillon, et al., Gapless Andreev bound states in the quantum spin Hall insulator HgTe, Nat. Nanotechnol. 12 (2017) 137–143.
[52] J. Wiedenmann, et al., 4π-periodic Josephson supercurrent in HgTe-based topological Josephson junctions, Nat. Commun. 7 (2016) 10303.
[53] K. Le Calvez, et al., Joule overheating poisons the fractional ac Josephson effect in topological Josephson junctions, Commun. Phys. 2 (2019) 4.
[54] P. Schuffelgen, et al., Selective area growth and stencil lithography for in situ fabricated quantum devices, Nat. Nanotechnol. 14 (2019) 825–831.
[55] I.T. Rosen, et al., Fractional AC Josephson effect in a topological insulator proximitized by a self-formed superconductor, Phys. Rev. B 110 (2024) 064511.
[56] C. Li, et al., 4π-periodic Andreev bound states in a Dirac semimetal, Nat. Mater. 17 (2018) 875–880.
[57] A. De Cecco, et al., Interplay between electron overheating and ac Josephson effect, Phys. Rev. B 93 (2016) 180505(R).
[58] C.D. Shelly, et al., Existence of Shapiro steps in the dissipative regime in superconducting weak links, Phys. Rev. Appl. 13 (2020) 024070.
[59] M.C. Dartiailh, et al., Missing Shapiro steps in topologically trivial Josephson junction on InAs quantum well, Nat. Commun. 12 (2021) 78.
[60] B.H. Elfeky, et al., Evolution of 4π-Periodic supercurrent in the presence of an In-Plane magnetic field, ACS Nano 17 (2023) 4650–4658.
[61] P. Zhang, et al., Missing odd-order Shapiro steps do not uniquely indicate fractional Josephson effect, SciPost Physics 18 (2025) 203.
[62] W. Liu, et al., Period-doubling in the phase dynamics of a shunted HgTe quantum well Josephson junction, Nat. Commun. 16 (2025) 3068.
[63] D. Averin, A. Bardas, Ac Josephson effect in a single quantum channel, Phys. Rev. Lett. 75 (1995) 1831–1834.

[64] G.E. Blonder, et al., Transition from metallic to tunneling regimes in superconducting microconstrictions: excess current, charge imbalance, and supercurrent conversion, Phys. Rev. B 25 (1982) 4515–4532.
[65] R. Haller, et al., Ac Josephson effect in a gate-tunable Cd_3As_2 nanowire superconducting weak link, Phys. Rev. B 108 (2023) 094514.
[66] D. Laroche, et al., Observation of the 4π-periodic Josephson effect in indium arsenide nanowires, Nat. Commun. 10 (2019) 245.
[67] R.S. Deacon, et al., Josephson radiation from gapless andreev bound States in HgTe-Based topological junctions, Phys. Rev. X 7 (2017) 021011.
[68] N. Abboud, et al., Signatures of Majorana bound states and parity effects in two-dimensional chiral p-wave Josephson junctions, Phys. Rev. B 105 (2022) 214521.